










# Diagnosing a Solar Flaring Core with Bidirectional Quasi-periodic Fast Propagating Magnetoacoustic Waves

Yuhu Miao<sup>1,2</sup> , Dong Li<sup>3</sup> , Ding Yuan<sup>1</sup> , Chaowei Jiang<sup>1</sup> , Abouazza Elmhamdi<sup>4</sup> , Mingyu Zhao<sup>5</sup> , and Sergey Anfinogentov<sup>6</sup> 

<sup>1</sup> Institute of Space Science and Applied Technology, Harbin Institute of Technology, Shenzhen, Guangdong 518055, People's Republic of China  
[miaoyuhu@hit.edu.cn](mailto:miaoyuhu@hit.edu.cn), [yuanding@hit.edu.cn](mailto:yuanding@hit.edu.cn)

<sup>2</sup> CAS Key Laboratory of Solar Activity, National Astronomical Observatories, Beijing 100012, People's Republic of China

<sup>3</sup> Key Laboratory of Dark Matter and Space Astronomy, Purple Mountain Observatory, CAS, Nanjing 210033, People's Republic of China

<sup>4</sup> Department of Physics and Astronomy, King Saud University, P.O. Box 2455, Riyadh 11451, Saudi Arabia

<sup>5</sup> Yunnan Observatories, Chinese Academy of Sciences, Kunming 650011, People's Republic of China

<sup>6</sup> Institute of Solar-Terrestrial Physics, 664033, Irkutsk, Russia

Received 2020 December 22; revised 2021 January 21; accepted 2021 January 22; published 2021 February 22

## Abstract

Quasi-periodic fast propagating (QFP) waves are often excited by solar flares, and could be trapped in the coronal structure with low Alfvén speed, so they could be used as a tool for diagnosing both the flaring core and magnetic waveguide. As the periodicity of a QFP wave could originate from a periodic source or be dispersively waveguided, it is a key parameter for diagnosing the flaring core and waveguide. In this paper, we study two QFP waves excited by a Geostationary Operational Environmental Satellite-class C1.3 solar flare occurring at active region NOAA 12734 on 2019 March 8. Two QFP waves were guided by two oppositely oriented coronal funnels. The periods of two QFP waves were identical and were roughly equal to the period of the oscillatory signal in the X-ray and 17 GHz radio emission released by the flaring core. It is very likely that the two QFP waves could be periodically excited by the flaring core. Many features of this QFP wave event are consistent with the magnetic tuning fork model. We also investigated the seismological application with QFP waves, and found that the magnetic field inferred with magnetohydrodynamic seismology was consistent with that obtained in the magnetic extrapolation model. Our study suggests that the QFP wave is a good tool for diagnosing both the flaring core and the magnetic waveguide.

*Unified Astronomy Thesaurus concepts:* [Active solar corona \(1988\)](#); [Solar flares \(1496\)](#); [Solar oscillations \(1515\)](#); [Solar coronal waves \(1995\)](#); [Solar coronal seismology \(1994\)](#); [Magnetohydrodynamics \(1964\)](#); [Solar coronal heating \(1989\)](#)

*Supporting material:* animation

## 1. Introduction

Quasi-periodic fast propagating (QFP) magnetoacoustic waves were first reported by Liu et al. (2011) with the full-disk imaging capability of the Atmospheric Imaging Assembly (AIA; Lemen et al. 2012) on board the Solar Dynamics Observatory (SDO; Pesnell et al. 2012). QFP waves propagate at local Alfvén speed across a distance on the scale of solar radius. Their periodicity appears to be consistent with the pulsating period of the light emission flux of a solar flare; therefore, they are believed to be excited by repetitive flaring energy releases (Liu et al. 2012; Shen & Liu 2012; Shen et al. 2013).

Yuan et al. (2013) found that the QFP wave trains were likely to be triggered by spiky flaring energy releases, and they suggested that QFP wave trains could be excited impulsively and evolve into a quasi-periodic nature with the wave guiding effect of magnetized coronal structure. This scenario was demonstrated by injecting impulsive energy into a diverging magnetic funnel. The quasi-periodic nature was well reproduced both in the trapped fast magnetoacoustic wave and the leaky mode (Pascoe et al. 2013, 2014; Qu et al. 2017). A number of studies supported the dispersive evolution of the fast magnetoacoustic wave within coronal waveguides (Nisticò et al. 2014; Shen et al. 2018; Miao et al. 2019, 2020).

Goddard et al. (2019) did a parametric study on the initial impulsive drive of QFP waves and found that the final spatial

and spectral signatures of the guided QFP wave trains depend strongly on the temporal duration of the initial perturbation. This dependence gives rise to the potential of diagnosing the flare core region with the excited QFP wave. Takasao & Shibata (2016) did a numerical magnetic reconnection experiment and showed that the flaring loop is bombarded by the backward flow from the reconnecting site. Such a recurring plasma flow created a magnetic tuning fork above the loop top. This region acts as an Alfvénic resonator and becomes a source of the quasi-periodic process, therein the QFP wave could leak from the loop top. This scenario was also justified with SDO/AIA's multitemperature observations (Takasao & Shibata 2016; Li et al. 2018).

QFP waves have a potential application in diagnosing the flaring core and its magnetic waveguide. Goddard et al. (2016) found that QFP wave trains could overrun the leading edge of coronal mass ejection (CME), and their interaction could modulate the radio emissions and generate quasi-periodic sparks in the radio spectrograph. This signal could supply the key information of the CME's expanding front. Ofman & Liu (2018) provide the first evidence of counter-streaming QFP waves that could potentially lead to turbulent cascade and dissipate sufficient energy flux for coronal heating in low-corona magnetic structures.

In this study, we aim to constrain the source of periodicity with a bidirectional QFP wave excited by a flare. The wave

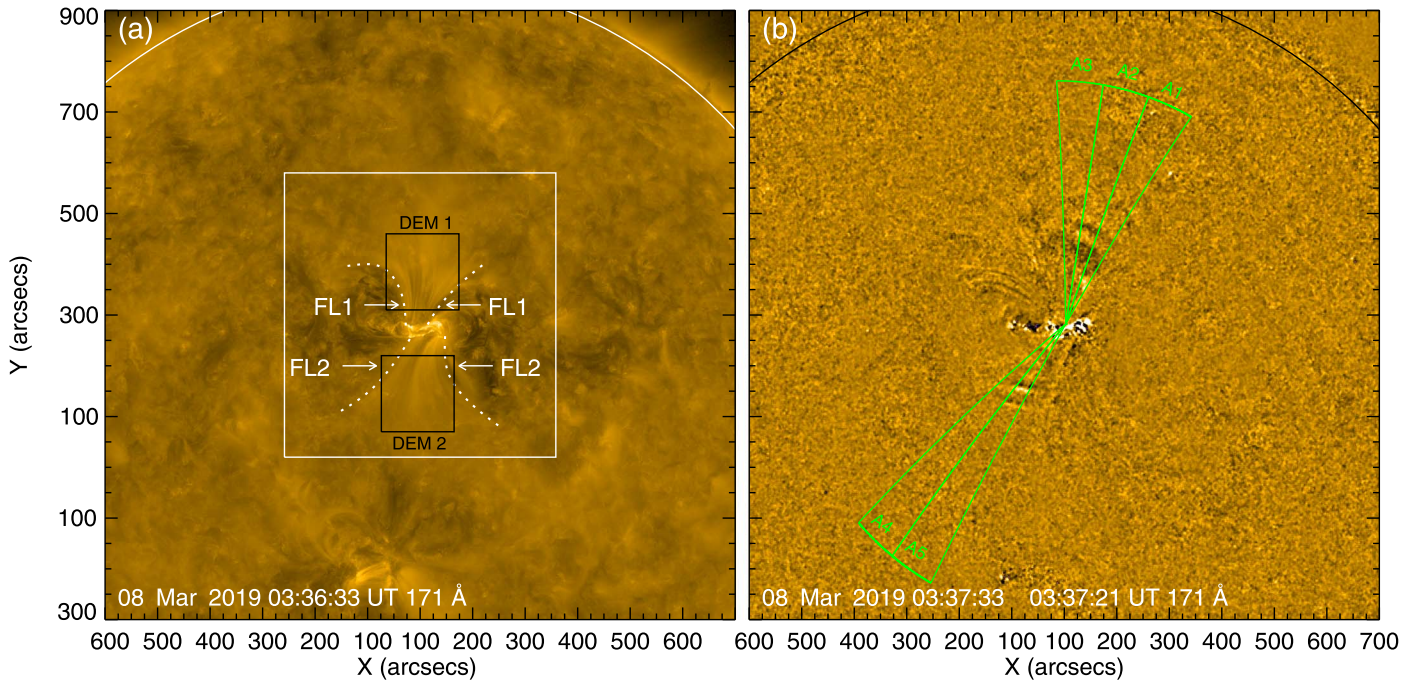


**Figure 1.** (a) AIA 171 Å image showing AR 12734 and the coronal funnels. Regions enclosed by DEM1 and DEM2 were used in the DEM analysis. FL1 and FL2 label the two coronal funnels used in this study. The white dotted lines indicate the borders of FL1 and FL2. The white rectangle indicates the region used in DEM analysis as shown in Figure 5. (b) Difference image of the AIA 171 Å channel to highlight wave propagation. An animation of this figure is available. It begins on 03:00:21 and ends at 04:04:21. The real-time duration of the animation is 6 s. Sectors A1–A5 were used to make time–distance plots shown in Figure 2.

(An animation of this figure is available.)

train and the flaring energy release exhibited identical periodicity. We propose the employment of the bidirectional QFP wave potential to constrain the origin of periodicity, and an investigation of the capability of plasma diagnostics. In Section 2, we describe the flare-triggered QFP event and the relevant data analysis. Section 3 presents the main results; the discussion and conclusions are given in Section 4.

## 2. Observations and Data Analysis

In this study, we analyzed a C1.3-class solar flare and the associated wave features originating from active region NOAA 12734 on 2019 March 8. The integrated X-ray flux over the range of 1–8 Å was recorded by Geostationary Operational Environmental Satellite (GOES). The GOES X-ray flux started to rise at 03:07 UT, reached maximum at 03:18 UT, and dropped off at around 04:00 UT. This flare had two emission peaks. During the first flaring peak, the eruption of a higher-lying filamentary structure excited a large-scale extreme ultraviolet (EUV) wave (see reviews by Chen 2011; Liu & Ofman 2014; Warmuth 2015). This EUV wave propagated radially from the flare epicenter, with the projected phase speed at about 200–600 km s<sup>-1</sup>. The second flaring peak triggered a pair of QFP waves. These two QFP waves propagated outwardly following two coronal funnels oriented to the north and south, respectively. The flaring process and the associated wave excitation is illustrated in Figure 1 (see the animation).

The C1.3-class solar flare and the associated EUV and QFP waves were recorded by SDO/AIA. We used the AIA 171 and 193 Å data to study this event. The AIA data were calibrated with the standard routine provided by the Solar Software, each image was normalized by its exposure time. An AIA image pixel corresponds to an angular width of 0".6; the image sequences in all AIA channels had a cadence of about 12 s.

To quantify the kinematics of the bidirectional QFP waves, we took the intensities along a slit with the origin located at the flare epicenter. To improve the signal-to-noise ratio, we averaged the intensity with a few neighboring pixels, the number of pixels used for the averaging was proportional to the distance to the flare epicenter. This technique is indicated by a set of five sectors labeled with “A1–A5” in Figure 1, each sector had an angular extent of 10°. The sectors were chosen to sample the QFP waves with significant amplitude. The spatially averaged intensities were stacked in order of time to form time–distance plots as shown in Figure 2. To highlight the wave propagation feature, we used the running-difference images. Each difference image was calculated by taking the backward difference with the image taken 12 s earlier.

To reveal the oscillatory signal of the QFP wave, we performed wavelet analysis (Torrence & Compo 1998; Feng et al. 2020; Liang et al. 2020; Wang et al. 2020) to the intensity variation at the position L1–L5 at sector A1–A5 (see Figure 2). We used the same method to analyze the period of the QFP wave train observed in the AIA 193 Å channel, (see Table 1). We also analyzed the derivative of GOES X-ray flux as well as the Nobeyama Radioheliograph (NoRH) 17 GHz data. The wavelet spectra are illustrated in Figure 3.

The QFP waves appeared to be guided by the open magnetic funnel; therefore, we did a nonlinear force-free field extrapolation to show the magnetic configuration of AR 12734 (Jiang et al. 2018; Zou et al. 2020). The boundary magnetogram was provided by SDO/HMI. We visualized the magnetic field lines from strong polarities at the AR 12734 to highlight funnel structures as displayed in Figure 4.

To estimate the plasma temperature and density of the coronal funnel, we used six EUV channels of SDO/AIA to calculate the differential emission measure (DEM), the code

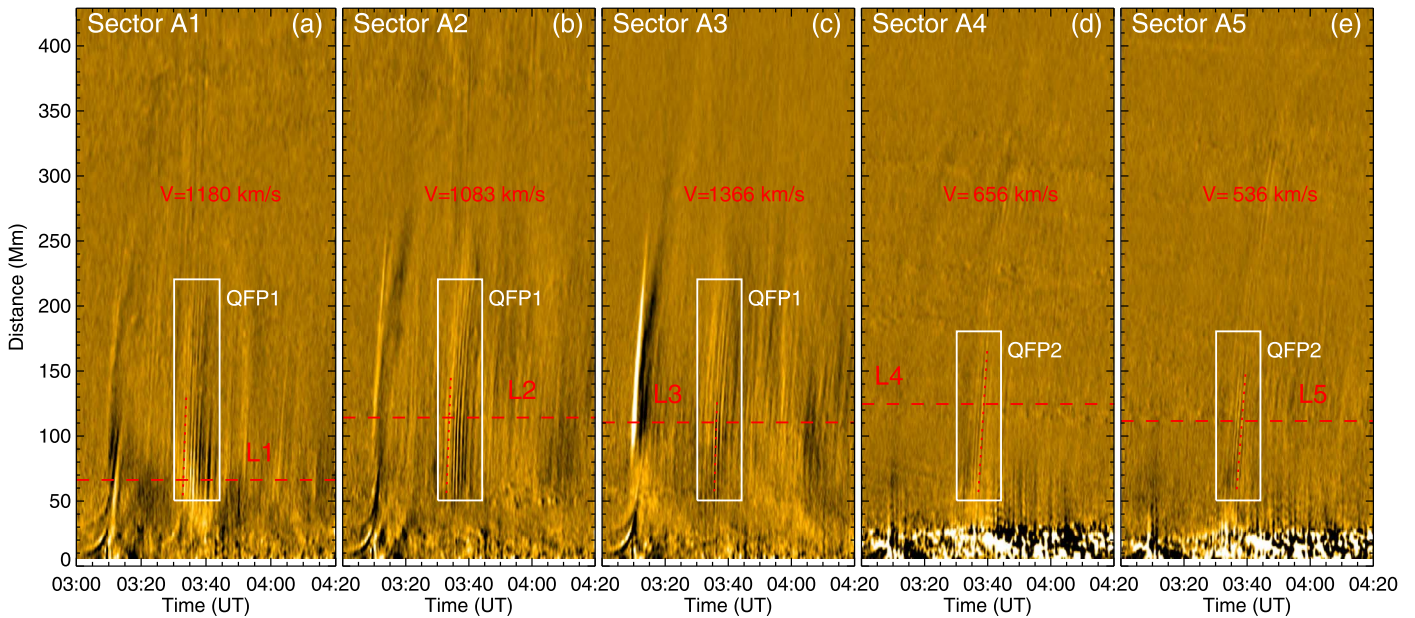


**Figure 2.** (a)–(e) time–distance diagrams corresponding to sectors A1–A5. The QFP wave features are indicated by the boxes. The red-dashed lines mark the positions used in wavelet analysis for period measurement. Each red dotted line within a white rectangle follows a sample QFP wave front, its slope was used to measure the propagating speed.

was developed by Cheung et al. (2015) and Su et al. (2018). The DEM inversion was done at 03:00 UT before the QFP wave excitation and 03:36 UT during this process. The DEM maps at different temperature ranges are plotted in Figure 5, which reveals the plasma emissions before and during the QFP wave propagation. To evaluate the plasma temperature and density of the coronal funnel, we selected two regions, labeled as DEM1 and DEM2 in Figure 1(a) and integrated the average DEM to calculate the emission measure (EM). The thickness of a coronal funnel was estimated within the magnetic field extrapolation model, it was about three times a typical width of a coronal loop observed at AR 12734. This thickness was used as an estimate of the column depth ( $d$ ) of the coronal plasma. Then, the electron density could be estimated using  $n = \sqrt{EM/d}$ .

### 3. Results

#### 3.1. Kinetics of the Bidirectional QFP Waves

Figure 2 reveals the propagation and periodicity of the bidirectional QFP waves. Sections A1–A3 were placed over coronal funnel 1 (FL1) and have captured the feature of QFP wave 1 (QFP1). We could see that the QFP1 wave propagated at speeds of 1083 to 1366 km s<sup>-1</sup>. The periods obtained at positions L1, L2, and L3 were  $66 \pm 22$  s,  $63 \pm 21$  s, and  $62 \pm 22$  s, respectively. These periodicities were measured in the wavelet spectrum, shown as an example in Figure 3.

Sectors A4 and A5 captured the features of QFP wave 2 (QFP2) propagating in coronal funnel 2 (FL2) in the AIA 171 Å channel. Their speeds were measured to be 656 km s<sup>-1</sup> and 536 km s<sup>-1</sup> at sectors A4 and A5, respectively. The periodicities at these two sectors were  $65 \pm 19$  s,  $66 \pm 19$  s, respectively. In the 193 Å channel, the projected propagation speeds were relatively smaller, the respective speeds were about 397 km s<sup>-1</sup> and 358 km s<sup>-1</sup>; the corresponding periods were  $73 \pm 19$  s and  $66 \pm 20$  s, respectively. The propagation speeds and periods are listed in Table 1.

#### 3.2. Periodicities of Flare Emission and QFP Waves

The bidirectional QFP waves followed two separate coronal funnels oriented in opposite directions. It appears that the two QFP waves exhibited identical periodicities, which could have a common origin from the flaring core. We use the light curve of soft X-ray emission and the 17 GHz radio emission integrated over AR 12734 to show the periodicity of the flaring core. In order to suppress the low-frequency spectral components, we removed the general trend in the 17 GHz radio emission signal, whereas for the X-ray emission flux, we take its time derivative for further analysis. Therefore, the periodicities on a minute timescale could be easily detectable.

Figure 3 implies that the detrended 17 GHz radio emission signal and the time derivative of the X-ray emission flux exhibited a periodicity at about one minute, the periods were about  $75 \pm 20$  s and  $79 \pm 20$  s, respectively. The periodic signal in the 17 GHz radio flux started to oscillate at about 03:29 UT and disappeared at about 03:34, the duration of periodicity was about 5 minutes, see Figure 3(g). The oscillatory signal in the GOES X-ray emission started at about 03:32 UT, lagging about 3 minutes behind the radio signal, see Figure 3(d). We note here that the GOES X-ray flux and the periodic fast wave started almost simultaneously.

#### 3.3. Magnetic Structure of the Coronal Funnels

Figure 4 displays the magnetic field lines originating from the strong polarities at AR 12734, where the magnetic structures of two coronal funnels were clearly seen. FL1 deviated about 30° from the plane of the boundary, whereas FL2 had a deviation angle of about 45°. We shall note that AR 12734 has an altitude of about 20°. Henceforth, after correcting the projection effect, we obtained that FL1 and FL2 deviated from the plane-of-the-sky for about  $\phi_1 = 10^\circ$  and  $\phi_2 = 65^\circ$ , respectively. The magnetic field strength was estimated at  $B_1^{\text{extr}} = (7 - 23)$  G for FL1 and  $B_2^{\text{extr}} = (4 - 22)$  G for FL2.

**Table 1**  
Parameters of the Bidirectional QFP Waves

Region	Wave	Channel	Slit	Phase Speed( km s <sup>-1</sup> )	Position	Period (s)
Coronal funnel 1	QFP1	171 Å	A1	1180	L1	66 ± 22
	QFP1	171 Å	A2	1083	L2	63 ± 20
	QFP1	171 Å	A3	1366	L3	62 ± 22
Coronal funnel 2	QFP2	171 Å	A4	656	L4	65 ± 21
	QFP2	171 Å	A5	536	L5	66 ± 19
	QFP2	193 Å	A4	397	...	73 ± 19
	QFP2	193 Å	A5	358	...	66 ± 20
Flaring core	NoRH	17 GHz	...	...	...	79 ± 20
	GOES	(1–8) Å	...	...	...	75 ± 20

Here we used extrapolated magnetic field to estimate the width of two coronal funnels, and found that both of them had a width of about 5 Mm, this value is about two to three times the typical width of a coronal loop in this active region. This value could be used as an estimate of the column depth for the coronal funnels; however, we shall consider the line-of-sight effect. Therefore, the column depth for FL1 is about  $d_1 = 5.1$  Mm and  $d_2 = 11.8$  Mm for FL2.

### 3.4. Plasma Temperature and Density

Figure 5 shows DEM maps at various temperature ranges from 0.3 to 8 MK. The flaring core consisted of hot plasma at a broad range of temperature from 1 to 8 MK. We shall note that during the QFP wave process, the flaring core was heated to high temperature as a whole (see Figure 5(h)), this pattern had a big contrast to the status before the QFP process, during which the flaring core had only hot plasma in the filamentary structure, see Figure 5(d). Two coronal funnels confined plasma mostly at temperatures around 0.3–0.9 MK.

The plasma temperature was calculated by locating the temperature where DEM reached its maximal value. FL1 and FL2 had an average temperature of about  $T_1 = 1.23$  MK and  $T_2 = 1.15$  MK, respectively.

We then integrated the DEM over temperature and obtained the EM. The DEM had two district peaks at low and high temperature ranges, the high temperature component may arise owing to the contribution of low-lying plasma structure, such as those seen in Figures 5(b) and (f). So, when we calculated the EM, the high temperature component was disregard, as in Li et al. (2020). We find that FL1 had an average electron number density at about  $4.86 \times 10^8 \text{ cm}^{-3}$  before the QFP and dropped to  $4.18 \times 10^8 \text{ cm}^{-3}$  when the QFP wave started to propagate along it. With the identical method, FL2 had a plasma with the average number density of electrons at about  $2.65 \times 10^8 \text{ cm}^{-3}$  before the flare and decreased to  $2.45 \times 10^8 \text{ cm}^{-3}$ .

### 3.5. Seismological Application

QFP waves propagated at an average speed of about  $v_1 = 1210 \text{ km s}^{-1}$  at FL1, if we correct the projection effect, the fast magnetoacoustic speed at FL1 was about  $v_{F1} = v_1 / \cos \phi_1 = 1230 \text{ km s}^{-1}$ . As FL1 had a plasma temperature of  $T_1 = 1.23$  MK, the acoustic speed was  $C_1 = 163 \text{ km s}^{-1}$  at coronal funnel FL1. Henceforth, the Alfvén speed at FL1 could be obtained,  $V_{A1} = 1220 \text{ km s}^{-1}$ . Here we assumed that the wavevector is parallel to the magnetic field vector. Considering  $v_2 = 596 \text{ km s}^{-1}$ ,  $\phi_2 = 65^\circ$ , and

$T_2 = 1.15$  MK, we obtained that the acoustic speed and Alfvén speed at coronal FL2, are about  $C_2 = 158 \text{ km s}^{-1}$  and  $V_{A2} = 1410 \text{ km s}^{-1}$ , respectively. In combination with the density estimates, the average magnetic fields for FL1 and FL2 are about  $B_1^{\text{seism}} = 12.8 \text{ G}$  and  $B_2^{\text{seism}} = 11.3 \text{ G}$ , respectively. The detailed parameters of plasma and magnetic field are listed in Table 2.

## 4. Discussion and Conclusions

In this paper, we analyze the oscillatory processes accompanying a C1.3 solar flare. The flare light curves in X-ray and radio emission both exhibited an oscillatory signal. Two QFP waves were launched from the flaring core, and propagated along two oppositely oriented coronal funnel structures. We took advantage of the unique magnetic structuring and studied the origin of the periodic signals, and investigated the potential seismological applications on the magnetized plasma and the flaring source.

In this event, the flaring core was an energy source of the QFP wave trains, whereas the coronal funnels acted as waveguides for the fast MHD waves. Fast magnetoacoustic waves could propagate across magnetic field lines, and the wave energy could be trapped by regions with low Alfvén speed (see Pascoe et al. 2013, 2014, for example). The QFP waves at two separate coronal funnels were found to have identical periodicity, see Table 1. The oscillatory signal of the flaring core was revealed in the X-ray and 17 GHz radio emission, with periods slightly greater than the period of the QFP waves. However, if we consider the uncertainties in the measurement, they could be considered as roughly equal. We should also bear in mind that the flare core generated spiky energy releases, which could make the spectral analysis less accurate. It should be noted that the difference in speeds between 171 and 193 Å channels are listed in Table 1. This difference might be caused by the inclination angle of coronal funnels with different temperatures.

We explored the seismological potential with DEM analysis, magnetic field extrapolation and MHD wave analysis. DEM analysis provides the thermal parameters of the plasma confined by the coronal funnels, i.e., plasma density and temperature. With the wave parameters, we could infer the Alfvén speed and henceforth the magnetic field strength. With magnetic field extrapolation, we obtained a reference that could be used to assess the accuracy and robustness of MHD seismology with QFP wave. With the geometric and magnetic parameters of the coronal funnels measured in the extrapolation, we find that the magnetic field strength obtained with

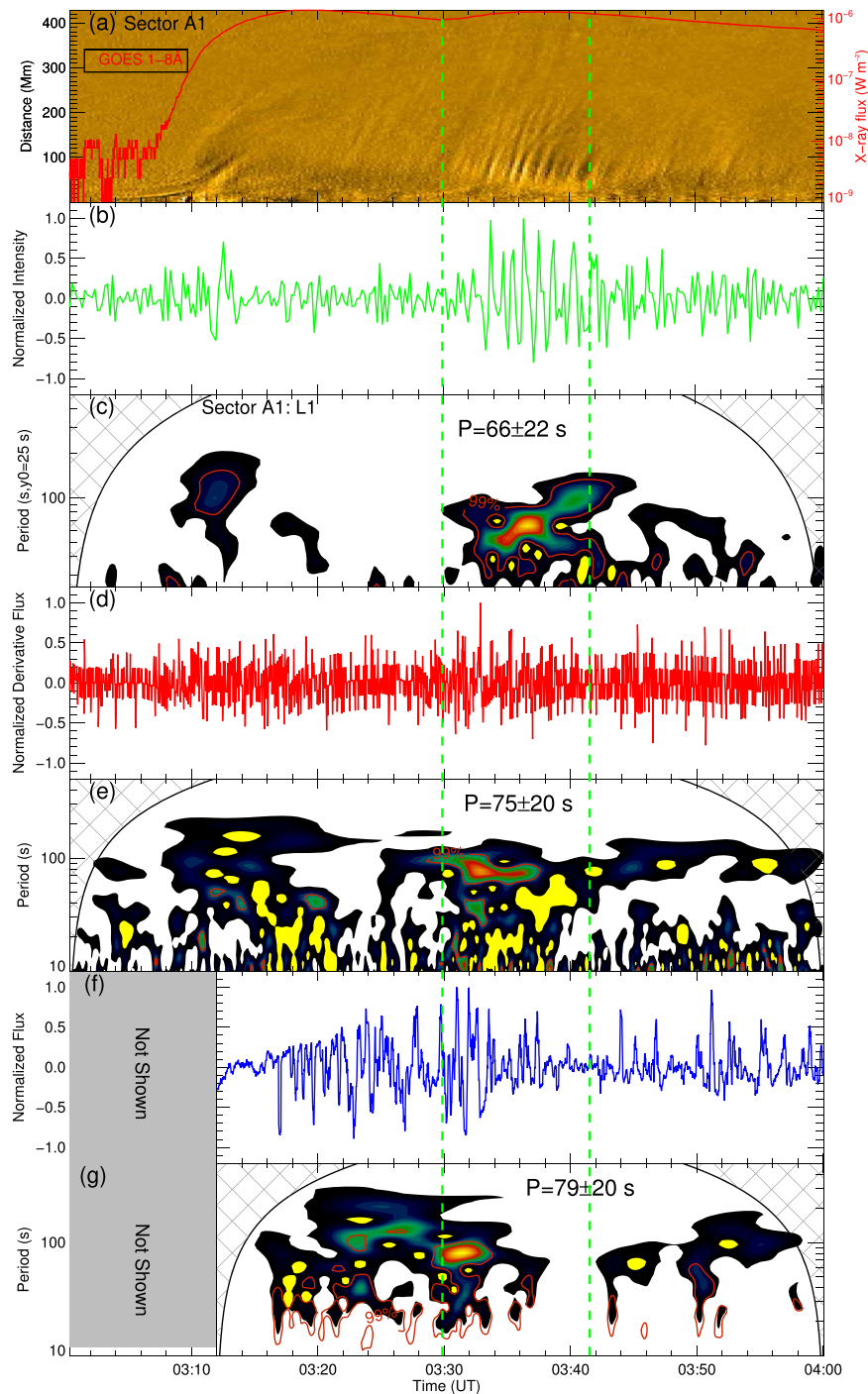


**Figure 3.** (a) Time–distance plot of Sector A1, overlaid with the GOES X-ray flux. (b)–(c) Detrended emission intensity measured at L1 in Figure 2(a) and its wavelet spectrum. (d)–(e) Derivative of GOES X-ray flux and its wavelet spectrum. (f)–(g) Detrended RoRH 17 GHz radio emission flux and its wavelet spectrum. The radio data of NoRH 17 GHz started at about 03:12 UT. The two green vertical dashed lines highlight the time interval of QFP wave and periodic signal in the flaring core. The  $y_0$  indicates the initial value of the Y-axis in panel (c).

MHD seismology agreed with the value measured in the magnetic field extrapolation model within a factor of about 0.5–2. This result is consistent with seismology applications with kink wave (Aschwanden & Schrijver 2011) and the numeric kink wave models (De Moortel & Pascoe 2009). We shall note that the magnetic field diverges with height, so the magnetic field strength obtained in MHD seismology is in fact the value averaged over the magnetic waveguide; therefore, the MHD seismology with QFP wave gives reasonable values.

Based on the above analyses, we could conclude that the QFP wave might be generated by an oscillatory signal at the flaring core. This scenario agrees in many aspects with the magnetic tuning fork model simulated by Takasao & Shibata (2016). The magnetic field at the coronal loop top could be bombarded by repetitive flow generated by magnetic reconnection above the loop arcade systems. A magnetic tuning fork is formed above the loop top, and becomes an Alfvénic resonator. The trapped fluid energy bounces back and forth within the

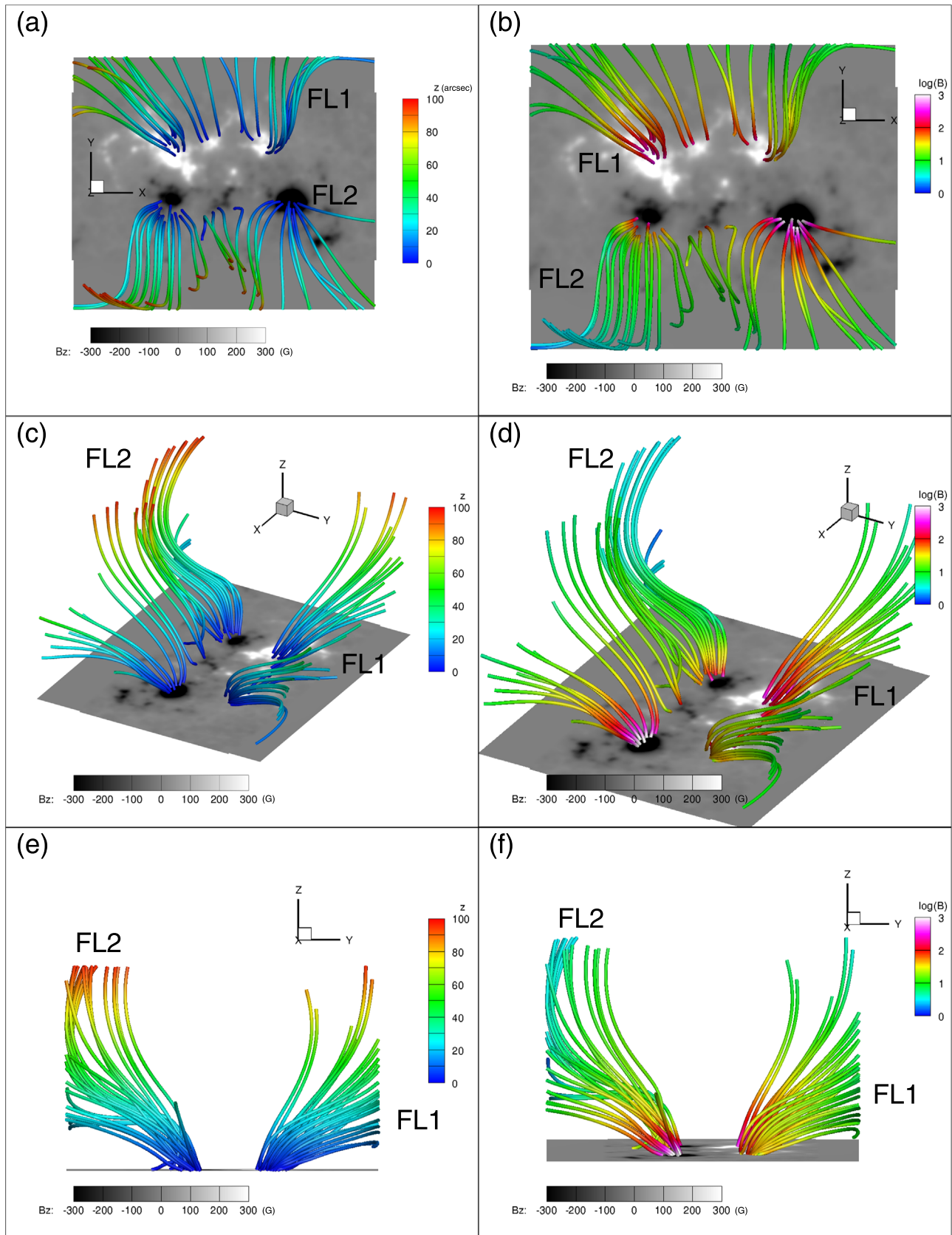


**Figure 4.** Nonlinear force-free magnetic field extrapolation. Panels (a)–(f) show the magnetic field line highlighting coronal funnels FL1 and FL2 at different viewing angles. The left column uses height as a color bar to show the magnetic field lines, whereas the right column uses field strength to label color. The FOV of the magnetogram is about  $340'' \times 200''$ .

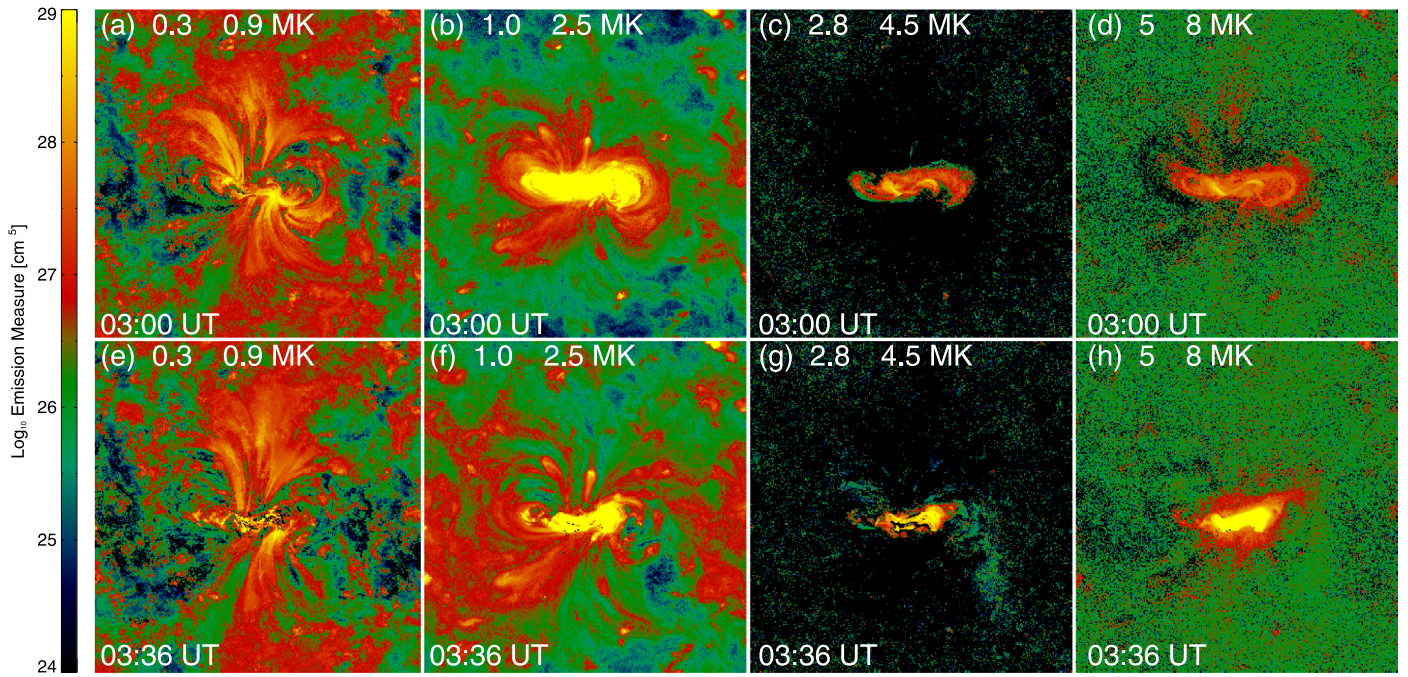


**Figure 5.** DEM maps as a function of temperature. Panels (a)–(d) show the DEM maps before the flare eruption at 03:00 UT. Panels (e)–(h) present DEM maps during the QFP wave propagation at 03:36 UT.

**Table 2**  
Parameters of the Plasma and Magnetic Field

Parameter	Value
Coronal Funnel 1	
Temperature [MK]	1.23
Number density of electrons [ $\text{cm}^{-3}$ ]	$4.18 \times 10^8$
Wave speed [ $\text{km s}^{-1}$ ]	1210
Fast speed [ $\text{km s}^{-1}$ ]	1230
Acoustic speed [ $\text{km s}^{-1}$ ]	163
Alfvén speed [ $\text{km s}^{-1}$ ]	1220
Angle with the boundary plane in extrapolation	$30^\circ$
Angle with the plane of sky	$10^\circ$
Magnetic field strength (extrapolation) [G]	7–23
Magnetic field strength (seismology) [G]	12.8
Coronal Funnel 2	
Temperature [MK]	1.15
Number density of electrons [ $\text{cm}^{-3}$ ]	$2.45 \times 10^8$
Wave speed [ $\text{km s}^{-1}$ ]	596
Fast speed [ $\text{km s}^{-1}$ ]	1410
Acoustic speed [ $\text{km s}^{-1}$ ]	158
Alfvén speed [ $\text{km s}^{-1}$ ]	1400
Angle with the boundary plane in extrapolation	$45^\circ$
Angle with the plane of sky	$65^\circ$
Magnetic field strength (extrapolation) [G]	4–22
Magnetic field strength (seismology) [G]	11.3






magnetic tuning fork, becoming a quasi-periodic signal. This is the source of periodicity at the X-ray and radio signals. A magnetic tuning fork could trap fast magnetoacoustic waves, and they could leak through the boundaries and become QFP waves guided by the coronal funnel that were rooted close to the magnetic tuning fork. We shall also note that the QFP waves could be generated directly by repetitive magnetic reconnections at the flaring core as observed by Li et al. (2018).

In this study, the bidirectional QFP waves provide a new possibility to diagnose the features of flaring core and coronal magnetic structures. Combining with DEM inversion and magnetic field extrapolation, the bidirectional QFP waves could be used to probe the features of the plasma waveguides in the solar atmosphere. As imaging observations are difficult to reveal the magnetic activities at the flaring core, MHD seismology with the periodic signal of QFP wave could be an alternative method to study the magnetic reconnection process above the loop top. This method is transferable to stellar flare investigation.

The authors thank the referee for valuable suggestions that improved the quality of the Letter. We are thankful for the excellent data provided by the SDO, GOES, and the Nobeyma. Y.H.M. and D.Y. are supported by the National Natural Science Foundation of China (NSFC, 11803005, 41731067), the Shenzhen Technology Project (JCYJ20180306172239618), the Shenzhen Science and Technology Program (Group No. KQTD20180410161218820), the China Postdoctoral Science Foundation (2020M681085) and the Open Research Program of the Key Laboratory of Solar Activity of Chinese Academy of Sciences (KLSA202110). D.L. is supported by the NSFC 11973092. C.W.J. is supported by the NSFC 41822404 and the Fundamental Research Funds for the Central Universities (grant No. HIT.BRETIV.201901). A.E. extends his appreciation to the Deanship of Scientific Research at King Saud University for funding this work through research group No. (RG-1440-092). M.Y.Z. is supported by the NSFC 11973086. We also thank C. Torrence and G. Compo for providing the wavelet software that is available at <http://atoc.colorado.edu/research/wavelets>.

#### ORCID iDs

Yuhu Miao <https://orcid.org/0000-0003-2183-2095>  
Dong Li <https://orcid.org/0000-0002-4538-9350>

Ding Yuan  <https://orcid.org/0000-0002-9514-6402>  
 Chaowei Jiang  <https://orcid.org/0000-0002-7018-6862>  
 Abouazza Elmhamdi  <https://orcid.org/0000-0002-5391-4709>  
 Mingyu Zhao  <https://orcid.org/0000-0002-3408-6549>  
 Sergey Anfinogentov  <https://orcid.org/0000-0002-1107-7420>

## References

- Aschwanden, M. J., & Schrijver, C. J. 2011, *ApJ*, 736, 102  
 Chen, P. F. 2011, *LRSP*, 8, 1  
 Cheung, M. C. M., Boerner, P., Schrijver, C. J., et al. 2015, *ApJ*, 807, 143  
 De Moortel, I., & Pascoe, D. J. 2009, *ApJL*, 699, L72  
 Feng, S., Deng, Z., Yuan, D., Xu, Z., & Yang, X. 2020, *RAA*, 20, 117  
 Goddard, C. R., Nakariakov, V. M., & Pascoe, D. J. 2019, *A&A*, 624, L4  
 Goddard, C. R., Nisticò, G., Nakariakov, V. M., Zimovets, I. V., & White, S. M. 2016, *A&A*, 594, A96  
 Jiang, C., Zou, P., Feng, X., et al. 2018, *ApJ*, 869, 13  
 Lemen, J. R., Title, A. M., Akin, D. J., et al. 2012, *SoPh*, 275, 17  
 Li, D., Yuan, D., Goossens, M., et al. 2020, *A&A*, 639, A114  
 Li, L., Zhang, J., Peter, H., et al. 2018, *ApJL*, 868, L33  
 Liang, B., Meng, Y., Feng, S., & Yang, Y. 2020, *Ap&SS*, 365, 40  
 Liu, W., & Ofman, L. 2014, *SoPh*, 289, 3233  
 Liu, W., Ofman, L., Nitta, N. V., et al. 2012, *ApJ*, 753, 52  
 Liu, W., Title, A. M., Zhao, J., et al. 2011, *ApJL*, 736, L13  
 Miao, Y., Liu, Y., Elmhamdi, A., et al. 2020, *ApJ*, 889, 139  
 Miao, Y. H., Liu, Y., Shen, Y. D., et al. 2019, *ApJL*, 871, L2  
 Nisticò, G., Pascoe, D. J., & Nakariakov, V. M. 2014, *A&A*, 569, A12  
 Ofman, L., & Liu, W. 2018, *ApJ*, 860, 54  
 Pascoe, D. J., Nakariakov, V. M., & Kupriyanova, E. G. 2013, *A&A*, 560, A97  
 Pascoe, D. J., Nakariakov, V. M., & Kupriyanova, E. G. 2014, *A&A*, 568, A20  
 Pesnell, W. D., Thompson, B. J., & Chamberlin, P. C. 2012, *SoPh*, 275, 3  
 Qu, Z. N., Jiang, L. Q., & Chen, S. L. 2017, *ApJ*, 851, 41  
 Shen, Y., & Liu, Y. 2012, *ApJ*, 753, 53  
 Shen, Y., Liu, Y., Song, T., & Tian, Z. 2018, *ApJ*, 853, 1  
 Shen, Y.-D., Liu, Y., Su, J.-T., et al. 2013, *SoPh*, 288, 585  
 Su, Y., Veronig, A. M., Hannah, I. G., et al. 2018, *ApJL*, 856, L17  
 Takasao, S., & Shibata, K. 2016, *ApJ*, 823, 150  
 Torrence, C., & Compo, G. P. 1998, *BAMS*, 79, 61  
 Wang, Z.-K., Feng, S., Deng, L.-H., & Meng, Y. 2020, *RAA*, 20, 006  
 Warmuth, A. 2015, *LRSP*, 12, 3  
 Yuan, D., Shen, Y., Liu, Y., et al. 2013, *A&A*, 554, A144  
 Zou, P., Jiang, C., Wei, F., et al. 2020, *ApJ*, 890, 10